

## Stephan's Quintet with XMM-Newton

G. Trinchieri<sup>1</sup>, J. Sulentic<sup>2</sup>, W. Pietsch<sup>3</sup>, and D. Breitschwerdt<sup>4</sup>

<sup>1</sup> INAF-Osservatorio Astronomico di Brera, via Brera 28, 20121 Milano, Italy  
e-mail: ginevra@brera.mi.astro.it

<sup>2</sup> University of Alabama, Tuscaloosa, AL 35487, USA

<sup>3</sup> Max-Planck-Institut für extraterrestrische Physik, Giessenbachstraße, 85740 Garching, Germany

<sup>4</sup> Institut für Astronomie, Universität Wien, Türkenschanzstr. 17, 1180 Wien, Austria

Received 21 February 2005 / Accepted 27 June 2005

### ABSTRACT

The prototype compact group known as Stephan's Quintet (SQ) was observed with XMM-Newton in order to complement the excellent resolution of *Chandra* with high sensitivity to extended emission. SQ is a dynamic environment whose main effect, at both X-ray and optical wavelengths, appears to be ISM stripping. This is manifested by: 1) secular evolution of morphological types towards earlier types and 2) growth of diffuse emission. Virtually all cold, warm, and hot gas in SQ is found outside of the member galaxies. XMM-Newton offers the opportunity to study the hot gas with unprecedented sensitivity. We find two main components: 1) extended high surface brightness emission from shocked gas associated with an ongoing collision and 2) even more extended and unrelaxed diffuse emission that follows the stripped stellar envelope of the group.

**Key words.** ISM: general – X-rays: galaxies – galaxies: ISM – X-rays: ISM

### 1. Introduction

Multi-wavelength data continue to accumulate for Stephan's Quintet (SQ) the most studied of the compact groups of galaxies. A framework for these observations has developed that may be quite generally relevant to the compact group phenomenon. Groups like SQ represent the densest galaxy aggregates in the non-clustered Universe. If SQ is representative, then compact groups evolve and grow through a process of sequential harassment by, and acquisition of, infalling intruder galaxies. It is not clear what stimulates the infall because the observed baryonic mass in SQ is about an order of magnitude too small to account for it. Two intruder galaxies have been identified in SQ (Moles et al. 1998). As summarized in Trinchieri et al. (2003), the older, and possibly captured, intruder (NGC 7320c) has left evidence of two passages in the form of parallel tidal tails. NGC 7319 was most likely the victim of the last passage, having lost most of its ISM. From the evidence of an "UV loop" in the new GALEX images of this system, Xu et al. (2005) suggest that only the older tail results from the passage of NGC 7320c, the younger one being caused by a close encounter with NGC 7318a. In either case, the Seyfert 2 nucleus in NGC 7319 may represent another manifestation of the encounter. Both it and NGC 7320c are examples of galaxies in transition from later (S) to earlier (E/S0) type. One or both of the members of SQ with elliptical morphology (NGC 7317 or 7318a) may have been stripped in earlier passages of the

old intruder. The "new" intruder (NGC 7318b) recently penetrated SQ at unusually high velocity ( $\Delta V \sim 1000 \text{ km s}^{-1}$ ), which suggests that it is not bound to the system. The strongest signs of current activity are related to this latter encounter.

The results of the active dynamical history in SQ yield multifold observational manifestations of the interaction process: 1) tidal deformations; 2) ISM stripping; 3) star formation suppression within the galaxies; 4) star formation sites in the stripped debris; 5) morphological transformations; 6) creation of a common halo of stripped stars; 7) shocks and, possibly, AGN ignition. It is widely assumed that interactions were more common in the early Universe, which makes detailed study of groups like SQ important beyond their benefit as laboratories for studying interaction physics. Signatures of the above interaction events have now been observed in all windows of the electromagnetic spectrum except the gamma ray. SQ might therefore become a reference for extragalactic observers.

Recent *Chandra* observations of SQ (Trinchieri et al. 2003) generally support the above evolutionary picture and have quite distinctly shown the effects of interaction between SQ and its intruders. A large scale shock ( $\sim 40 \text{ kpc}$  at  $85 \text{ Mpc}$ ) seen in both ROSAT-HRI and *Chandra* images as a prominent narrow NS feature embedded in more complex and extended diffuse emission is further confirmed by these XMM-Newton observations (Fig. 1). The NS structure was found to be distinctly clumpy and sharply bounded on the W side. Spatial coincidence of the X-ray shock is found with both radio

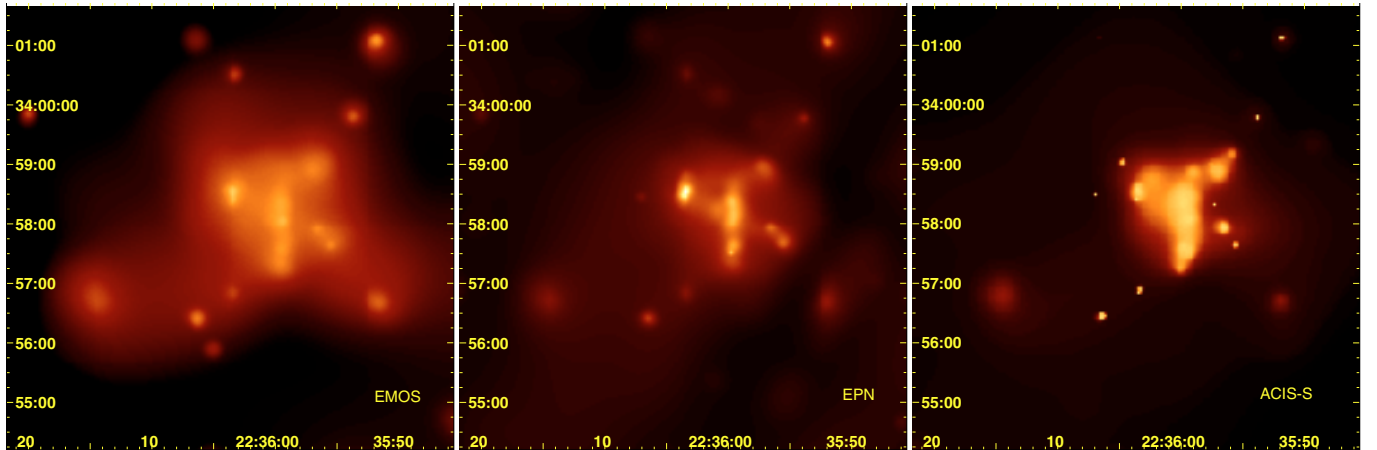


**Fig. 1.** Comparison of XMM-Newton EPIC-MOS and EPIC-pn images with *Chandra*-ACIS in the 0.3–3 keV band. MOS1 and MOS2 are merged. Adaptive smoothing is applied using *csmooth* in the *Ciao* package (see <http://asc.harvard.edu>). XMM images show lower resolution but enhanced sensitivity to extended emission.

continuum (Williams et al. 2002) and forbidden [NII] emission (Sulentic et al. 2001), while little correspondence is seen between the X-ray and optical broad band images. The principal X-ray features are best explained as manifestations of the shock produced by collision of the new intruder with the debris field produced by passages of the old intruder. However, if the stripped ISM of NGC 7319 was largely displaced towards the east, in the direction of NGC 7320c, as suggested by the observed HI distribution (Williams et al. 2002), then the currently shocked debris field must be the product of an earlier encounter between the old intruder and, perhaps, NGC 7318a. The NS X-ray feature was interpreted (Trinchieri et al. 2003) as a bow shock propagating through the pre-existing debris field and heating it to a temperature of  $\sim 0.5$  keV. The low temperature of the post-shock is a problem unless we postulate: a) an oblique shock and/or b) a weak shock where the upstream medium is hot and has a sizable counter-pressure. As discussed in Trinchieri et al. (2003), a standard weak shock is unlikely, given the high Mach number of the inflowing gas in the frame of reference of the new intruder. In order to reduce the post-shock temperature to a value consistent with that derived from X-ray spectral fitting, the gas would have to enter the shock with respect to the shock surface at an angle of  $30^\circ$  or less. This will only happen at the wings of the bow-shock.

In Trinchieri et al. (2003) we estimated the cooling time from X-ray spectral fitting and a standard cooling function for a low metallicity plasma in collisional ionization equilibrium to be roughly  $4 \times 10^8$  yr for a mean density of  $n_X \sim 2.7 \times 10^{-2} \text{ cm}^{-3}$ . Note that in the surrounding upstream medium the density can be lower by a factor of 5–10, so that cooling can be completely negligible, but that denser regions in the shock have higher densities and correspondingly shorter cooling times.

This interpretation is attractive because it would also better explain evidence that the new intruder shows considerable tidal distortion. In this case *in flagrante delicto* implies an intruder crossing time of  $t_c \sim 10^8$  years.

**Table 1.** Log of the XMM-Newton observations for Stephan’s Quintet.

Instrument	Livetime (s)	
	Total	Used
EPIC-pn	37 088	31 531
EPIC-MOS1	44 845	36 775
EPIC-MOS2	44 833	36 766

## 2. XMM-Newton data analysis

SQ was observed for  $\sim 40$  ks with EPIC-MOS and EPIC-pn during revolution 366 of XMM-Newton. The event files were reprocessed with the *xmmsas*–5.4.1 release and further cleaned of residual high background due to flaring activity. We used the EPIC-pn light curve for processing data from all instruments. Only photons with FLAG = 0 and PATTERN  $\leq 4$  (for EPIC-pn), or PATTERN  $\leq 12$  (EPIC-MOS), were used in the analysis. The final exposure times for the accepted events are listed in Table 1. Data analysis employed both the *xmmsas/ftools* and *ciao/funtools* tasks with heavy reliance on ds9 and corollary software.

### 2.1. X-ray Images: characterization of the diffuse emission

In an effort to enhance the signal-to-noise, we merged the central CCD frames of the two EPIC-MOS observations and smoothed the result with an adaptive algorithm (*ciao* – *csmooth*). EPIC-pn data are kept separate because of the different patterns of CCD gaps in EPIC-pn and EPIC-MOS instruments. EPIC-pn, EPIC-MOS, and *Chandra* (Trinchieri et al. 2003) images (0.3–3.0 keV) are compared in Fig. 1, which illustrates the complimentary power of data from the two satellites. While the *Chandra* image clearly shows more discrete features, the large collecting area of XMM-Newton facilitates detection of diffuse X-ray emission components. A comparison of EPIC-MOS emission in different energy bands

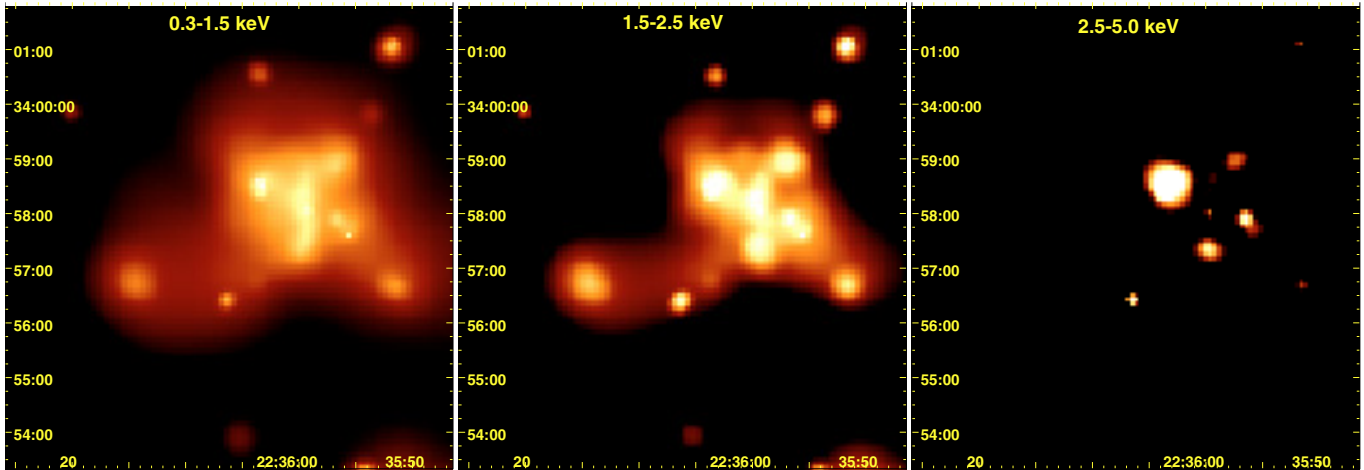


**Fig. 2.** Comparison of smoothed EPIC-MOS images in the 0.3–1.5 keV (*left*), 1.5–2.5 keV (*center*), and 2.5–5.0 keV (*right*) bands. Extensive diffuse emission is evident in the softest image.

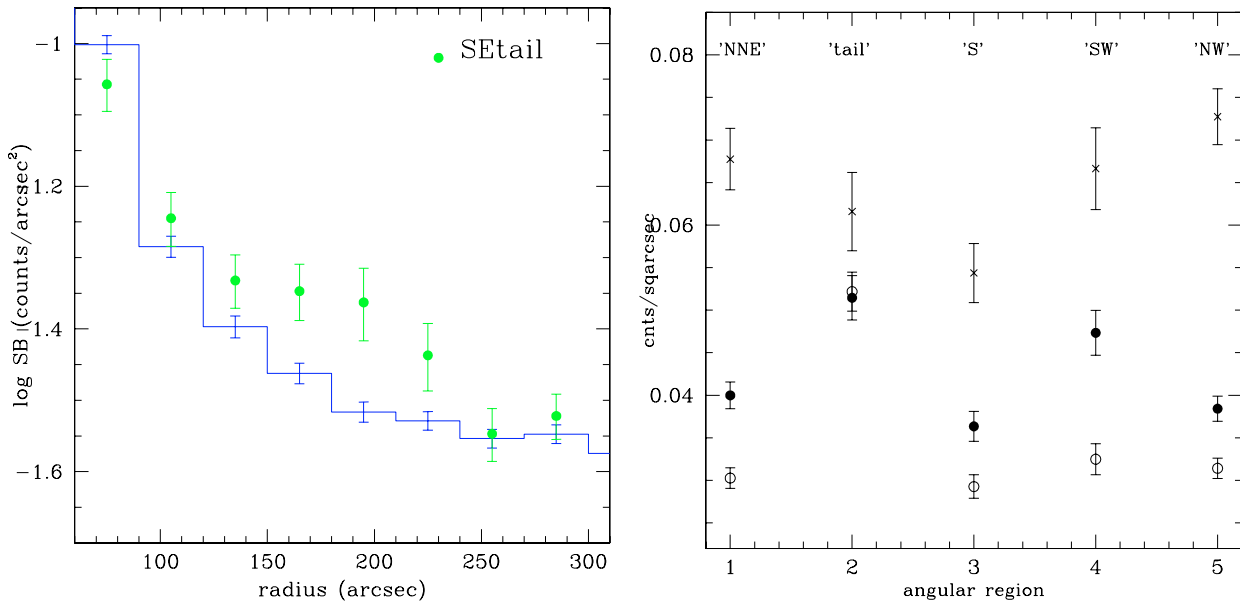


**Fig. 3.** *Left:* the radial distribution of X-ray emission in the azimuthal ranges  $95^{\circ}$ – $140^{\circ}$  (filled dots, SEtail) and complementary  $140^{\circ}$ – $95^{\circ}$  (histogram), obtained from the combined EPIC-MOS data (0.3–2.5 keV) that are free of CCD gaps. The former shows the excess diffuse emission in the direction of the tidal tails. *Right:* azimuthal distribution of the emission at different radial distances from the middle blob in the NS feature: Crosses:  $r = 75''$ – $114''$ ; Filled dots:  $r = 114''$ – $180''$ ; empty dots:  $r = 180''$ – $240''$ . The sources associated with the Seyfert NGC 7319 and with NGC 7317 are masked out. Azimuthal angles are: NNE =  $0^{\circ}$ – $95^{\circ}$ ; tail =  $95^{\circ}$ – $140^{\circ}$ ; S =  $140^{\circ}$ – $210^{\circ}$ ; SW =  $210^{\circ}$ – $255^{\circ}$ ; NW =  $255^{\circ}$ – $360^{\circ}$ .

is shown in Fig. 2. Both figures reveal the complexity of the emission in SQ with a multitude of both compact and extended features centered on the NS oriented shock, with different relative strengths as a function of the energy band considered (see later). A previously undetected component is visible towards the SE as an extension that connects the low surface brightness emission at the center of the group with an enhancement that was marginally detected in the *Chandra* data (Trinchieri et al. 2003). This new component, called TAIL for easy reference in the text, is faint even in XMM-Newton images making a full characterization of its properties very difficult.

The more sensitive XMM-Newton data allow a better definition of low surface brightness emission in SQ, and we have

tried to determine its extent by means of radial profiles of the X-ray emission. Regions of CCD gaps, bad columns, and bad pixels identified on the exposure maps are masked, and all detected sources outside a radius of  $\sim 3'$  from the center of SQ are excluded. Emission above  $\sim 2.5$ – $3.0$  keV is associated with the nucleus of NGC 7319 and a few much fainter individual sources. Diffuse emission is detected out to a maximum extent of  $r \sim 4'$  at energies below  $\sim 2.5$  keV. However, the emission becomes clearly nonuniform with increasing distance from the central shock region, so that the extent depends on the assumed direction. Figure 3 shows both the clear excess in the TAIL region identified above (left panel) and the azimuthal dependence of the extent of the emission (right panel), towards the

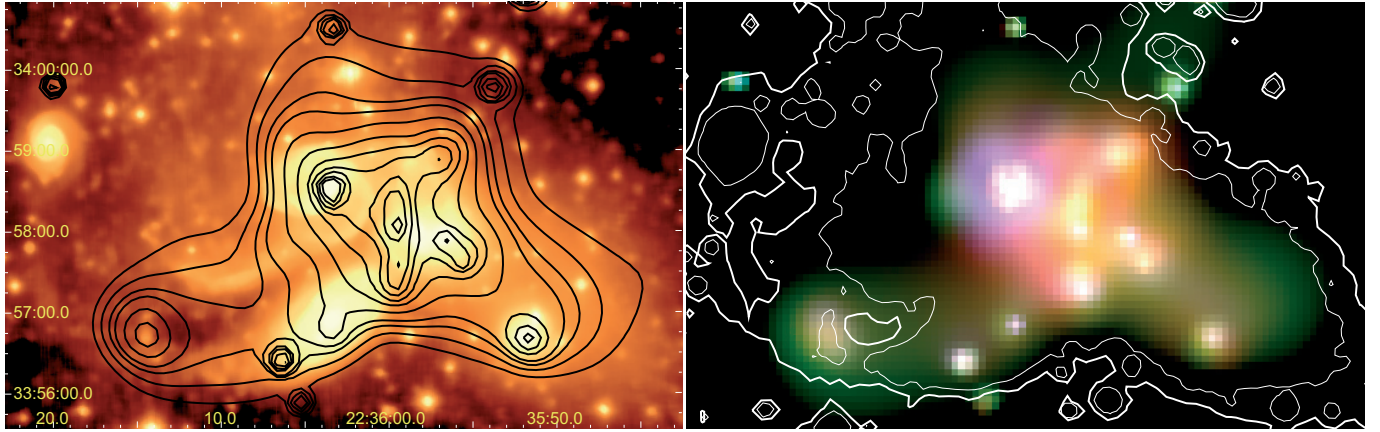


**Fig. 4.** (Left) Merged EPIC-MOS contours superimposed on a deep *R*-band image taken at the 2.5 m INT (courtesy of Carlo Gutiérrez). The 0.3–3.0 keV band X-ray data were smoothed with an adaptive algorithm before contouring. Outer contours chosen to show maximum extent of X-ray emission. (Right) Optical *R* band contours superimposed on a “true” color X-ray image produced from 3 different EPIC-MOS energy bands: red: 0.3–1.5 keV; green = 1.5–2.5 keV; blue = 2.5–6.0 keV. Contours were chosen to show maximum extent of the diffuse halo.

SE (TAIL) and the SW (towards NGC 7317) at an average radius of  $2'–3'$ . The smaller extent towards S could reflect the presence of additional absorption, due also in part to the foreground NGC 7320; however, the same should be true for TAIL. The EPIC-MOS CCD gaps make any characterization of any diffuse structure outside  $r \sim 4'$  difficult to quantify properly.

In order to better highlight different spectral signatures in the complex emission from SQ, we generated a color image combining data in three broad bands: 0.3–1.5, 1.5–2.5, and 2.5–7.0 keV (displayed as red, green, and blue, respectively). The resulting image, shown in Fig. 4, shows a number of localized regions with different colors that imply differences in photon energy distribution. Many of these regions lack sufficient photons for a detailed spectral analysis but we can make a rough comparison of the relative photon distributions for some of the regions that are illustrated in Fig. 5. A more detailed analysis is given for regions with high enough photon statistics (see Sect. 2.2). Constant broad energy bins are used for constructing all of the “pseudo-spectra” displayed in Fig. 6. These energy distributions have not been corrected for instrumental response. They were extracted from relatively small areas of the central CCD in EPIC-MOS, so we do not expect variations in the response matrix to affect this qualitative comparison between different sources and regions, but cannot be used to derive spectral shapes.

The pseudo-spectra show significant differences that suggest these sources are unlikely to be fit with the same spectral model. We comment on the most striking:

1. Regions B and C (top panel) show similar distributions especially compared with region A. The average pseudo-spectrum of the shock region is intermediate between A and B distributions. *Chandra* data suggest that a compact source (*Chandra* #5 Trinchieri et al. 2003) is embedded in condensation C (but not at its center). With the current astrometry and published positions of the  $H\alpha$  knots (e.g. Xu et al. 2003), the *Chandra* position does not suggest coincidence with any obvious optical feature in the new intruder, so it might be an unrelated background source. A region of

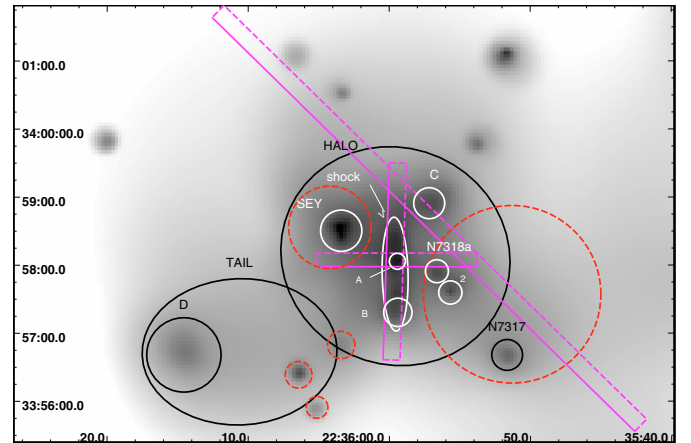


**Fig. 5.** Identification of source regions used in the production of pseudo-spectra (Fig. 6). Unlabeled red regions within a marked area were excluded from the spectral analysis of that region. Also shown are the regions used to produce the cuts shown in Figs. 9 and 10.

intense star formation (STARBURST A in Xu et al. 1999) and associated HI and CO emission lie between the N end of the shock and source C.

2. The sources in the middle panel are associated with SQ galaxies and show similar pseudo-spectra. NGC 7319 shows a strong hard photon excess which is most likely related to an obscured active nucleus. Significantly different line-of-sight absorbing column densities might explain the large difference between the lowest energy points of NGC 7318a and NGC 7317. This is consistent with the lack of any radio line or continuum detections near to NGC 7317. Unresolved radio continuum emission is detected from NGC 7318a (Williams et al. 2002; Xu et al. 2003). Source # 2 is also included in this panel. This is the only one of four very large ( $D \sim 400$  pc)  $H\alpha$  emission condensations detected as a discrete X-ray source (Trinchieri et al. 2003) and belongs to NGC 7318b (Sulentic et al. 2001).

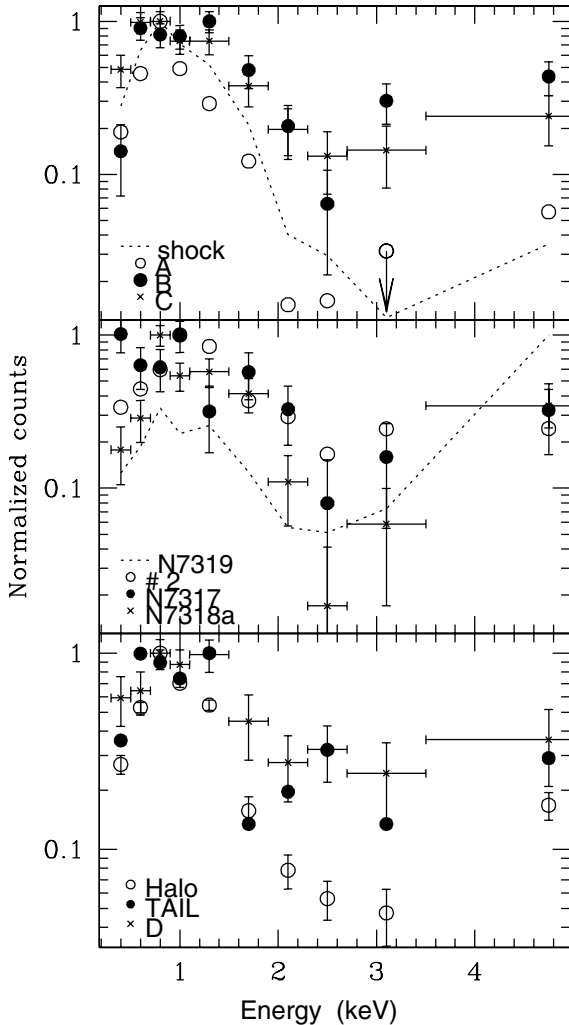


**Fig. 6.** Photon energy distributions (pseudo-spectra) for regions highlighted in Fig. 5. No correction for the spectral response is applied, so plotted distributions are not representative of the real spectral shapes. Counts are binned all in the same energy ranges (shown by horizontal bars) and normalized to the highest value so that relative shapes are immediately comparable to one another. Uncertainties are given only for selected regions to preserve clarity in the plots. Photons from smaller regions included in larger ones are not included in pseudo-spectra for these latter. *Top*: regions in or near the central shock region. *Middle*: Sources associated with SQ galaxies plus the single detected giant emission region SW of NGC 7318a (# 2). Because of the much stronger emission from the Seyfert nucleus of NGC 7319 in the hard band, that determines the relative normalization of the pseudo-spectrum, all points are systematically below other objects. *Bottom*: regions of diffuse emission outside the central shock region.

3. Diffuse emission regions outside the central shock region (bottom panel) do not show identical spectra: TAIL and D are consistent with each other but not with HALO. The latter feature is more reminiscent of the spectral distribution of the shock front and may be evidence for a larger scale of the shocked new intruder disk. This will complicate any inferences about the extent and integrated properties of diffuse X-ray component that existed before the arrival of the new intruder. It is unclear if D is a condensation near the end of this tail or an unrelated background source: there is

evidence of an extended object at its center (redshift and nature unknown at the present time), but at the same location there is a clear deficit in the HI distribution that, if foreground, would represent a smaller absorbing column with consequent local enhancement of the emission. The location of D also coincides with the “end” of the HI in Arc-S (Williams et al. 2002) and could also represent the edge of the expansion of the hot gas. The similarity of the spectral distributions for D and TAIL might favor interpretation of D as a feature associated with the more diffuse component in TAIL.

## 2.2. Characterization of individual features

The previous images and pseudo-spectra enable us to identify emission regions where it is possible to derive both the contribution of individual components (see Table 2) and where the photon energy distribution allows a more detailed spectral analysis. Table 2 lists detected counts, fluxes, and luminosities for individual sources detected and already presented in Fig. 5 for which a more detailed spectral analysis is not possible. Regions with stronger emission are instead considered for more detailed spectral modeling, as summarized in Table 3. Source shapes and sizes were adjusted to avoid regions of non-uniform illumination (e.g. CCD gaps), but were kept as large as possible (compatible with colors and morphologies implying coherent components, as suggested by both our X-ray color image and Fig. 6) in order to improve the signal-to-noise in the derived spectra. Photons were binned to achieve a minimum signal-to-noise  $\geq 2-3$  (depending on the resulting number of bins) in each energy bin after background subtraction. We generated *arf* and *rmf* files, using the most recent calibrations. We used  $\text{PATTERN} \leq 12$  for EPIC-MOS[1-2] (singles, doubles, triples, and quadruples) and  $\text{PATTERN} = 0$  for EPIC-pn (singles only), since we are mainly interested in softer energies where the “single” percentage was highest. We also considered “doubles” in the Seyfert data that contains many photons at higher energies, in order to increase the signal-to-noise. Results of spectral modeling are summarized in Table 3. The data do not provide meaningful constraints on the choice of spectral model, with several different assumptions yielding equally good results. In particular, we made two different assumptions for the abundance parameter, fixing it at 30% of cosmic (consistent with the choice in Trinchieri et al. 2003), and at 100%. The former value gives in general better fits, i.e., lower  $\chi^2$  values: an additional component is needed to obtain a similar  $\chi^2$  under the assumption of 100% cosmic. We chose a power law with fixed slope at  $\Gamma = 1.7$ , but other choices give equal results. The spectral parameters are generally consistent in the two models. In fact the error regions are ill-defined in several cases, due to apparent non-monotonicity in the  $\chi^2$  space. As discussed later (see also Trinchieri et al. 2003), the spectral parameters should be regarded as only indicative, as all regions are probably complex and might contain different components at different temperatures. Moreover, plasma temperatures are derived from models of optically thin emission, in which the plasma is assumed in collisional ionization equilibrium. In the

**Table 2.** Net counts in the 0.3–3 keV energy band in the PN and m1+m2 detector for selected regions, also shown in Fig. 5. The background is taken from an ellipse to the E, in a neighbouring CCD in EPIC-pn (see text). Fluxes and luminosities (0.3–3.0 keV band) are computed assuming a conversion factor of  $4 \times 10^{-17}$ , for EPIC-pn counts, corresponding to a line-of-sight value for absorption and a power law with  $\Gamma = 1.7$ , and a distance of 85 Mpc.

Src. #	Chandra <sup>1</sup> name	Position (J2000)	radius "	PN counts and error	MOS counts and error	flux cgs	luminosity cgs
1	1	22:35:53.96, +33:59:45.9	11.25	$73.2 \pm 10.2$	$58.7 \pm 8.9$	$2.9 \times 10^{-15}$	$2.5 \times 10^{39}$
2	2	22:35:55.68, +33:57:35.9	10.25	$186.5 \pm 14.1$	$97.7 \pm 10.3$	$7.5 \times 10^{-15}$	$6.5 \times 10^{39}$
NGC 7318a	3	22:35:56.47, +33:57:54.7	10.15	$218.9 \pm 15.2$	$129.0 \pm 11.7$	$8.8 \times 10^{-15}$	$7.7 \times 10^{39}$
NGC 7317	– <sup>2</sup>	22:35:51.66, +33:56:40.8	19.60	$101.9 \pm 11.1$	$90.9 \pm 10.3$	$4.1 \times 10^{-15}$	$3.1 \times 10^{39}$
C	5	22:35:57.18, +33:58:54.7	13.70	$337.7 \pm 19.0$	$217.4 \pm 14.3$	$1.4 \times 10^{-14}$	$1.2 \times 10^{40}$
D	– <sup>2</sup>	22:36:14.55, +33:56:41.0	13.60	$285.3 \pm 21.2$	$204.3 \pm 17.8$	$1.1 \times 10^{-14}$	$1.0 \times 10^{40}$
NGC 7320nuc	6-7	22:36:03.41, +33:56:49.7	12.10	$88.4 \pm 10.3$	$49.9 \pm 7.8$	$3.5 \times 10^{-15}$	$6.0 \times 10^{37\dagger}$
NGC 7320SE	11	22:36:06.42, +33:56:23.5	11.80	$118.7 \pm 11.7$	$83.4 \pm 9.8$	$4.8 \times 10^{-15}$	$8.3 \times 10^{37\dagger}$

<sup>†</sup> In NGC 7320, so we assume a distance of 12 Mpc.

<sup>1</sup> Positional coincidence. However the sizes of the XMM-Newton regions might include a larger fraction of extended emission.

<sup>2</sup> Not detected by Chandra.

presence of non-equilibrium plasma, such as in cases of shocks, these models would have the effect of “artificially” requiring a multi-temperature fit.

The background is chosen from a region to the E in the adjacent chip for EPIC-pn (but within the same CCD for EPIC-MOS), where we see and expect no emission from SQ. We also considered other regions to the N and W (also in adjacent EPIC-pn CCDs) but found no significant variations. Table 3 also lists the luminosities of the different regions for the different best fit parameters. In a few cases, where the best fit absorption is different, the softer band luminosity could be significantly different in the 30% and 100% abundance assumption.

**SHOCK region.** The shock region is a clumpy NS-oriented elongated feature (Fig. 5). This structure is similar to the one observed with *Chandra*. It includes condensations A and B but not C. The new X-ray data require a two temperature plasma, at  $\sim 0.3$  and  $\sim 1$  keV with  $N_H$  relatively high ( $3 \times$  the line-of-sight value).

Modeling the whole region is of limited significance given the differences observed in the photon spectral distributions of the sub-regions highlighted by the color image and the pseudo-spectra (Figs. 4–6). Analysis of different condensations within the shock confirms their different spectral properties. We considered three separate regions as indicated in Table 3 corresponding to the three main peaks determined by *Chandra* and confirmed in XMM-Newton. The middle one is larger than, but inclusive of, A. Assuming plasma models again, the middle and southern blob can be modeled with a single temperature but with different values for  $kT$  (0.6 and 0.2 keV respectively) and significantly different line-of-sight  $N_H$ . This may in part reflect the larger HI column ( $>6 \times 10^{20}$  atoms  $\text{cm}^{-2}$ ; Williams et al. 2002) along the line of sight due to the foreground galaxy NGC 7320 that partially covers the southern tip of the shock region.

A hard excess is visible in the data for region A (Fig. 7), regardless of the abundance parameter, which can be accounted

for by a second component (any model will do), even though the fit does not formally require a two component model ( $\chi^2_{\min} \sim 1$ ). No equivalent component is required in the other regions (except for the 100% abundance assumption, but see above). A two temperature model, with a relatively high amount of absorbing material, is instead required for the northern tip.

**HALO region.** All high surface brightness regions related to the shock, as well as discrete sources identified in Fig. 5, were excluded from the photon distribution yielding our best attempt to isolate a pure halo component. A two temperature model could represent the data, as in the previous region, but with a marginally credible  $\chi^2 = 262$  for 198 Degrees of Freedom, and high temperature values of  $kT_1 = 0.6$  and  $kT_2 = 4.2$  keV, with lower than galactic absorption  $N_H = 0.04$  (for 30% cosmic abundance; at 100% cosmic,  $\chi^2 = 274$ , for similar spectral parameters). Addition of a third component brings a significant improvement in the fit quality and the temperature values closer to those observed in other regions (see Table 3). In particular, the addition of a power law component gives a  $\Delta\chi^2$  of 45–55 (30–100% abundance respectively) for 2 additional parameters.

There is a likely possibility of contamination from discrete sources; one such was detected by *Chandra*, # 4 in Trinchieri et al. 2003, but not by XMM-Newton. However contamination should affect all regions equally, and we have subtracted all visible sources, so any contamination should be of a low level.

**TAIL region.** Counts from both source D and the connecting region were considered in order to improve the signal-to-noise. This combination is supported by the pseudo-spectra plot (Fig. 6) that indicates a similar photon distribution for the two features. On the other hand, it could be dangerous because we do not know if D belongs to SQ. Even taking this risk, we still have a small number of photons and the resulting parameters are not well determined. Although a single temperature model could be marginally acceptable ( $\chi^2_{\min} = 1.4$  for 34 d.o.f.), the best fit parameters ( $N_H$  significantly smaller than the

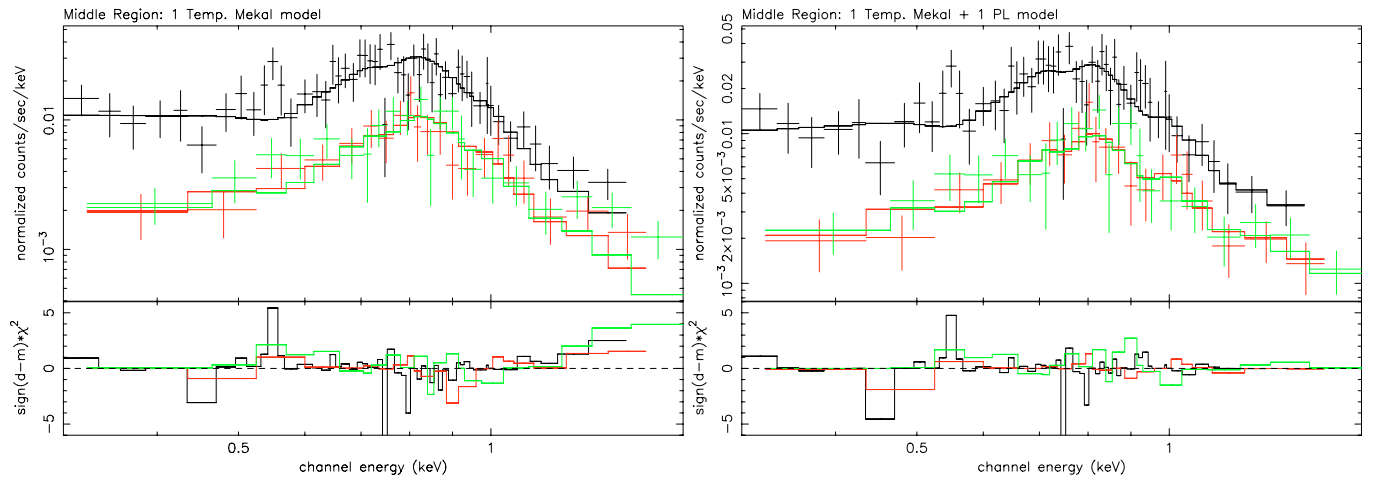
**Table 3.** Spectral results for the different regions defined in the text. The thermal model is a mekal with the stated percentage of cosmic abundance.

Region (cf. Fig. 6)				Counts and errors							
Z	$N_h$	$kT_1$	$kT_2$	$N_h$	$\Gamma$	$\chi^2(\text{d.o.f.})$	$\chi^2_\nu$	$L(\text{Total})$	$L(\text{Total})$	$L(kT_1)$	$L(kT_2)$
%	$\text{cm}^{-2}$	keV	keV	$\text{cm}^{-2}$				[0.5–2.0]	[2.0–10.0]	[0.5–2.0]	[0.5–2.0]
								$\text{erg s}^{-1}$	$\text{erg s}^{-1}$	$\text{erg s}^{-1}$	$\text{erg s}^{-1}$
SHOCK (includes A, B)				PN: $1558 \pm 40$ MOS1: $585 \pm 25$ MOS2: $613 \pm 25$							
30	0.28	0.25	0.84	–	–	195.6 (195)	1.0	$2.4 \times 10^{41}$	$4.1 \times 10^{39}$	$1.9 \times 10^{41}$	$4.7 \times 10^{40}$
100	0.36	0.23	0.98	–	–	214.9 (195)	1.1	$3.5 \times 10^{41}$	$4.1 \times 10^{39}$	$3.2 \times 10^{41}$	$3.9 \times 10^{40}$
100	0.19	0.27	0.81	–	1.7*	193.6 (194)	1.0	$1.4 \times 10^{41}$	$2.5 \times 10^{40}$	$1.4 \times 10^{41}$	$2.1 \times 10^{40}$
In shock: Southern Tip				PN: $337 \pm 19$ MOS1: $110 \pm 11$ MOS2: $99 \pm 10$							
30	0.49	0.22	–	–	–	46.5 (42)	1.11	$1.8 \times 10^{41}$	$4.9 \times 10^{37}$		
100	0.49	0.22	–	–	–	48.3 (42)	1.15	$1.7 \times 10^{41}$	$5.1 \times 10^{37}$		
In shock: Middle Region (~A)				PN: $470 \pm 21$ MOS1: $177 \pm 13$ MOS2: $207 \pm 15$							
30	0.03*	0.59	–	–	–	87.6 (93)	0.95	$2.0 \times 10^{40}$	$5.6 \times 10^{38}$		
30	0.07	0.50	–	–	1.7*	65 (92)	0.7	$2.5 \times 10^{40}$	$1.5 \times 10^{40}$	$1.6 \times 10^{40}$	
100	0.03*	0.59	–	–	–	122 (93)	1.31	$1.9 \times 10^{40}$	$3.8 \times 10^{38}$		
100	0.04	0.50	–	–	1.7*	65 (92)	0.7	$2.2 \times 10^{40}$	$1.4 \times 10^{40}$	$1.5 \times 10^{40}$	
In shock: Northern Tip				PN: $527 \pm 23$ MOS1: $207 \pm 15$ MOS2: $183 \pm 14$							
30	0.16	0.30	1.06	–	–	89.1 (72)	1.24	$2.0 \times 10^{40}$	$1.9 \times 10^{39}$	$1.2 \times 10^{40}$	$8.2 \times 10^{39}$
100	0.32	0.24	1.27	–	–	98.2 (72)	1.36	$9.8 \times 10^{40}$	$2.4 \times 10^{39}$	$8.5 \times 10^{40}$	$1.3 \times 10^{40}$
100	0.11	0.32	0.93	–	1.7*	86.4 (71)	1.21	$3.2 \times 10^{40}$	$1.3 \times 10^{40}$	$1.8 \times 10^{40}$	$6.5 \times 10^{39}$
HALO				PN: $2820 \pm 63$ MOS1: $1184 \pm 42$ MOS2: $1157 \pm 42$							
30	0.12	0.30	0.77	–	1.58	216.6 (196)	1.1	$1.9 \times 10^{41}$	$5.3 \times 10^{40}$	$9.5 \times 10^{40}$	$7.1 \times 10^{40}$
100	0.12	0.29	0.76	–	2.20	219.2 (196)	1.12	$1.8 \times 10^{41}$	$4.1 \times 10^{40}$	$8.6 \times 10^{40}$	$5.4 \times 10^{40}$
TAIL (Includes D)				PN: $441 \pm 33$ MOS1: $227 \pm 23$ MOS2: $210 \pm 23$							
30	0.42	0.16	1.50	–	–	33 (32)	1.05	$1.6 \times 10^{41}$	$1.0 \times 10^{40}$	$1.4 \times 10^{41}$	$2.5 \times 10^{40}$
100	0.72	0.1*	1.44	–	–	35 (32)	1.09	$1.7 \times 10^{42}$	$1.1 \times 10^{40}$	$1.6 \times 10^{41}$	$3.4 \times 10^{40}$
Seyfert galaxy**				PN: $3310 \pm 57$ MOS1: $993 \pm 32$ MOS2: $1029 \pm 32$							
30	0.04	0.60	–	45	1.33	421 (401)	1.05	$8.3 \times 10^{41}$	$2.7 \times 10^{42}$	$2.5 \times 10^{40}$	$2.6 \times 10^{42**}$
100	0.02	0.60	–	48	1.48	425 (401)	1.06	$1.1 \times 10^{42}$	$2.9 \times 10^{42}$	$2.0 \times 10^{40}$	$2.9 \times 10^{42**}$

## NOTES

\* Fixed value of  $\Gamma$ , and fixed lower limit for  $N_H$  or  $kT$ .

\*\* For the EPIC-PN data we used both single and double events. Intrinsic luminosities refer to total (all three components), plasma (0.5–2.0 keV band), and nuclear components (2–10 keV band), respectively.

**Fig. 7.** Spectral energy distribution for the central part of the shock including condensation A. *Left*: a single temperature plasma model is used to fit the data (see Table 3). *Right*: a power law is added to the model. The best fit temperature and galactic absorptions vary slightly from the original fit but are consistent within the errors.

line-of-sight value,  $kT > 2$  keV) are probably unreasonable for the system. A two component model gives a significantly better fit ( $\Delta\chi^2 > 14$  for 2 additional parameters yielding an  $f$ -test probability  $P > 99.99$  that the additional model component give an improved fit). Table 3 presents the results for a 2-plasma model fit. Equivalent results are found with plasma+thermal or plasma+power law models.

**NGC 7319.** The spectrum of NGC 7319 is clearly complex and requires several components, as we already found in our *Chandra* analysis. We now know that the discrete *Chandra* source #9 located 8 arcsec S of the nucleus is a  $z = 2.2$  QSO (Galianni et al. 2004), however, it contributes only about 5% of the photons near to NGC 7319. The Seyfert nucleus was fit with a double power-law and appropriately red-shifted FeK $\alpha$  line (see also Trinchieri et al. 2003). The slope of the power law can in principle be better constrained now because of the higher signal-to-noise at high energy. We find, however, that the complex spectrum requiring a model with several independent components and large absorbing column density gives too small a leverage for an accurate determination of the continuum. We also note that the region around the FeK line is not well modeled with the possibility of additional line components. At lower energies the data require a thermal plasma model with  $T \sim 0.6$  keV and no absorption above the galactic value, in agreement with the more tentative *Chandra* results. The Seyfert nucleus dominates the emission at all energies. At soft energies (0.2–2 keV) the unabsorbed power law and plasma components contribute equally while above 2 keV only the nuclear power-law source is present.

### 3. Discussion

Owing to the large effective area of the telescope, the XMM-Newton observations reveal new faint X-ray features in SQ that have hitherto been missed with *Chandra*. In addition, improved photon statistics allow determination of spectral components to higher accuracy, although we still cannot properly understand the real physical state of the gas, most likely because it is highly inhomogeneous and possibly not in collisional equilibrium.

XMM-Newton observations support most of the conclusions based on the *Chandra* observations and add confidence to some of the more tentative suggestions that were proposed. The complexity of the X-ray morphology is reinforced by similarly complex spectral characteristics. Nearly all *Chandra* sources are detected again by XMM-Newton (allowing for the degraded spatial resolution), and we can identify additional interesting features. Each of the principal emission features in the central region of SQ will be briefly discussed here with emphasis on new issues raised by the XMM-Newton observations.

#### 3.1. X-ray emission from SQ member galaxies

The central regions of most SQ members are now X-ray detected with luminosities above  $10^{39}$  erg s $^{-1}$ . The exceptions involve the old (NGC 7320c) and new (NGC 7318b) intruders. NGC 7320c is far from the current center of activity and shows no detectable HI or X-ray emitting gas. The case of

NGC 7318b, at the site of current impact, is more complex, and might be strongly related to the SHOCK itself (see discussion in the next section). Remnants of the HI disk of NGC 7318b are still recognizable, but no X-ray emission clearly associated with the central regions of this galaxy is detected. Only one of four bright emission line regions belonging to its southern spiral arm (Sulentic et al. 2001) is detected (source #2), at a luminosity of  $\sim 7 \times 10^{39}$  erg s $^{-1}$ . While high, examples of luminosities such as this are now found in increasing number associated with star-forming regions (Zezas et al. 1999; Roberts & Warwick 2000; Fabbiano et al. 2001; Zezas & Fabbiano 2002; Wolter & Trinchieri 2004). Several models suggest that interaction/collisions could enhance the star formation activity in galaxies (e.g. Jog & Solomon 1992; Fujita & Nagashima 1999; Bekki & Couch 2003), so the real question becomes what distinguishes this from the other bright regions nearby: perhaps this is simply denser/more compact or the first to evolve.

Both intruders, like NGC 7319 before them, are most likely undergoing transformation from late-type spiral to early-type E/S0 morphologies. Perhaps NGC 7317 and 7318a underwent a similar process in past epochs. The older optical tidal tail with apparently associated HI may be a manifestation of that past activity. Given its “field” (i.e. low galaxy surface density) environment, SQ is rich in early-type galaxies and will soon grow even richer. This appears to be one of the characteristics of compact groups at least as defined by the Hickson (1982) catalog. The stripping events creating early type galaxies has given rise to large quantities of cold (Williams et al. 2002) and hot diffuse gas. The stripping events involving the intruders were apparently efficient enough to prevent the fueling of any nuclear activity so far. NGC 7319 is the exception and shows a “typical” Seyfert 2 nuclear spectrum that can be modeled by a double power-law with  $\Gamma \sim 1.3$  plus a heavily absorbed component. The derived power-law slope is flatter than inferred from the *Chandra* data but consistent with spectra of other Seyfert 2s (della Ceca et al. 1999; Moran et al. 2001). A thermal component is required to account for excess at low energies. This was also suggested by the *Chandra* data, in particular when the contribution from a circumnuclear region of more extended emission is included in the spectrum. XMM-Newton resolution means that any nuclear spectrum includes the circumnuclear region, and a negligible one from the high  $z$  quasar (see Galianni et al. 2004).

#### 3.2. The shock

The sharp NS feature between NGC 7318ab and NGC 7319 shows a complex morphology with equally intriguing spectral characteristics. Higher resolution *Chandra* data showed several condensations and a steep W edge to the emission. These features are confirmed by XMM-Newton albeit with lower resolution. Comparison with data at other wavelengths illustrates the complexity of the shock region with shock-related effects prominent at radio (van der Hulst & Rots 1981; Williams et al. 2002; Xu et al. 2003), X ray (Pietsch et al. 1997; Sulentic et al. 2001; Trinchieri et al. 2003), and H $\alpha$ + [NII]. Some of the H $\alpha$ + [NII] emission shows a star formation signature (both

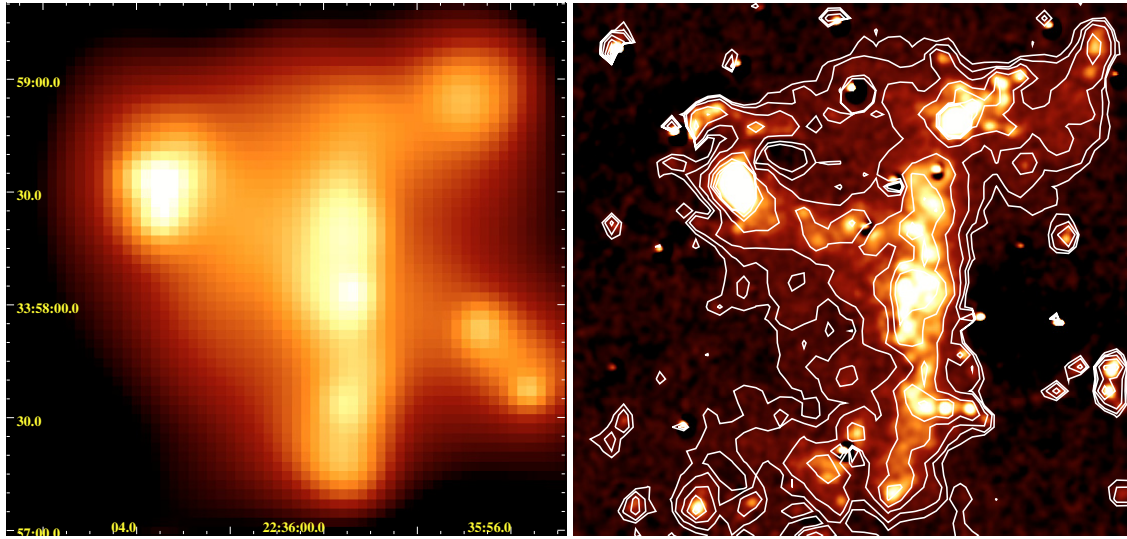


**Fig. 8.** Comparison between X-ray (smoothed EPIC-MOS data in 0.3–3.0 keV band, *Left*) and  $H\alpha+[NII]$  ( $\sim 6600 \text{ km s}^{-1}$ , *Right*) emissions in SQ. The emission at the bottom of the right panel, to the SE of the bright NS feature, is contaminated by  $[SII]\lambda 6717,6731$  emission in NGC 7320 that falls in the filter passband.

at SQ and new intruder velocities), which is now also seen in the UV (Xu et al. 2005). Examination of the high resolution Hubble images indicate that condensations A and B (Fig. 5) correspond to places where the spiral arms of NGC 7318b are visibly disrupted: in A, where one of them intersects the shock, one can see a clear detachment of the inner part of this arm dominated by stellar light (emerging from the central bulge) from the gaseous component. This can reasonably be assumed to correspond to a region of higher gas density in the new intruder disk. Higher resolution *Chandra* data suggest that B is spatially coincident with a relatively compact radio continuum feature (see e.g. Xanthopoulos et al. 2004) near the south end of the shock. An optical spectrum (Gallagher et al. 2001) shows the onset of shock induced line smearing at the same location (with new intruder velocities merging into SQ velocities).

A close correspondence between X-ray and  $H\alpha+[NII]$  emission was already noted in Trinchieri et al. (2003) and is again evident in the comparison with the XMM-Newton data in Fig. 8. Our interference filter image records both  $H\alpha$  and  $[NII]\lambda 6583$  emission. The association with the shock front is seen only in the  $H\alpha+[NII]$  emission with SQ velocities ( $\sim 6600 \text{ km s}^{-1}$ )<sup>1</sup>. Figure 8-left shows two strong concentrations of line emission coincident with the Seyfert nucleus of NGC 7319 and the shock front. There is also evidence of an extended lower surface brightness emission component extending mostly eastward from the shock front, which we will discuss later. The multiwavelength morphological similarities are signatures of a close link between different phases of the new intruder ISM and SQ IGM.

The 1D intensity cuts along the shock front (Fig. 9, top panels) show more quantitatively the remarkable correspondence between X-ray and line emission. The cuts are centered on A

as indicated in Fig. 5. The total extents of the emissions are comparable to a rather sharp boundary at  $\sim 50''$  S in all panels. The X rays appear slightly more extended towards the N as more clearly shown with the EPIC-MOS data. A good correspondence between line and X-ray emission is seen between  $30''$ – $50''$  to the S, while the  $H\alpha$  peak at  $-40''$  N, related to starburst A (Xu et al. 1999), does not show a corresponding X-ray feature. The nearby weaker X-ray peak is due to the contribution of component C, which partially enters our cuts, but is actually displaced from the position of the  $H\alpha$  maximum and extends towards the NW. Starburst A is coincident with an X-ray minimum, as well as an apparent  $H I/CO$  maximum. This probably means that the starburst has occurred recently, with supernova activity still to come.

The steep W boundary of the X-ray shock front discovered with *Chandra* motivated us to suggest a NE to SW transverse component of new intruder motion. Its presence in the X-ray data is difficult to understand in the context of shocks (see Trinchieri et al. 2003). A similarly sharp W boundary of the optical line emission reinforces the significance of this feature and the strong link between X-ray and  $H\alpha+[NII]$  emitting gas. The sharp drop is already evident in the  $H\alpha$  image (Fig. 8) but is dramatic in the 1D intensity cuts perpendicular to the shock front shown in Fig. 9 (bottom panels). Several examples of sharp X-ray boundaries have now been observed in clusters and groups (i.e. “cold fronts”, Mazzotta et al. 2002; Vikhlinin et al. 2001). However, in these, the spatial discontinuity is thought to correspond to a significant temperature decrease, while SQ does not show this effect. Both drops in X-rays and  $H\alpha$  could instead correspond to a (pre-existing) density discontinuity. This in turn implies that both emissions derive from impact with the same debris field. It is also conceivable that the X-ray discontinuity corresponds to a contact discontinuity where two separate flows are colliding. In that case, pressure and velocity would be continuous across the

<sup>1</sup> SQ and new intruder velocity ranges are  $V > 6000$  (mostly  $6300$ – $6600$ )  $\text{km s}^{-1}$  and  $5400$ – $6000$   $\text{km s}^{-1}$ , respectively (Xu et al. 1999; Sulentic et al. 2001).

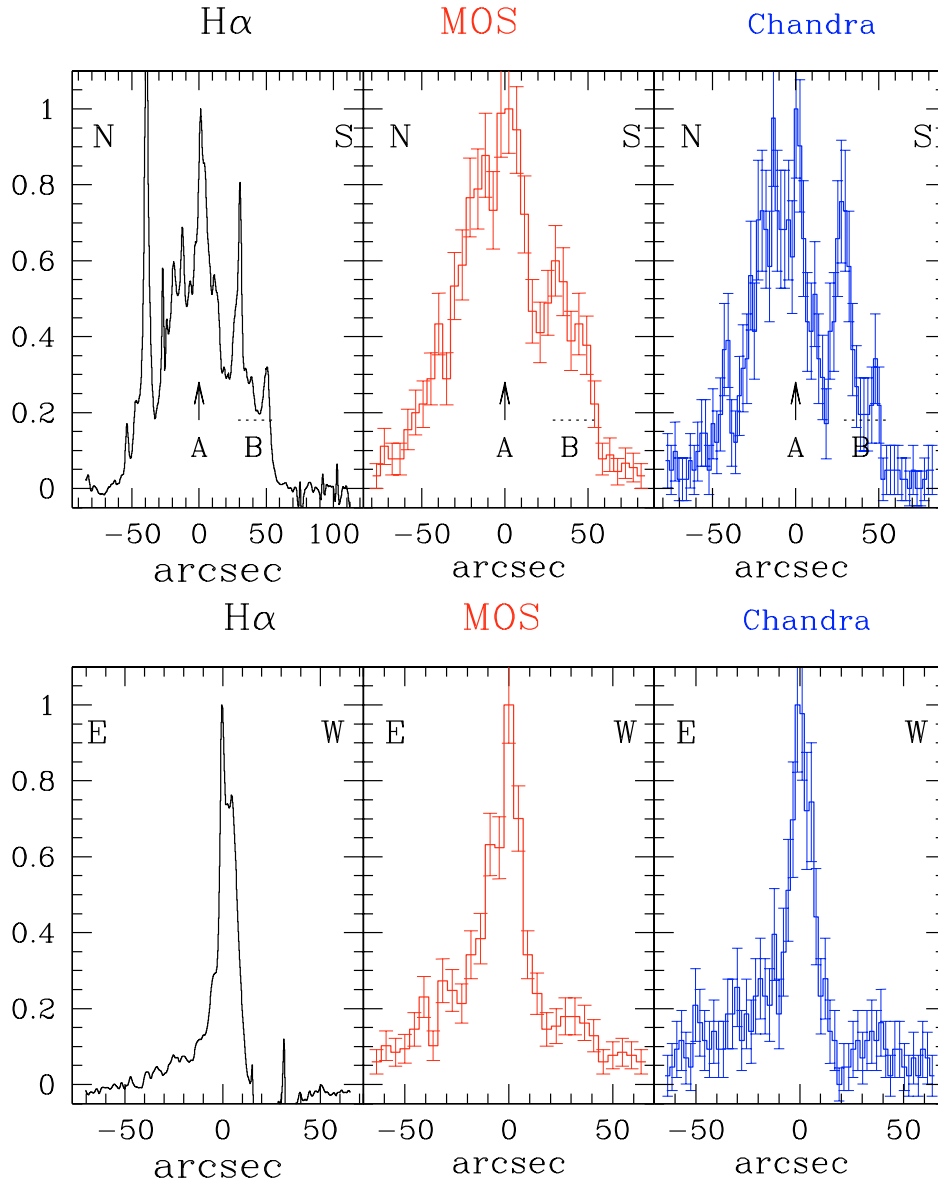


**Fig. 9.** (*Top*) Intensity plots of the  $H\alpha$ + $[N\text{II}]$  and X-ray images (0.3–3.0 keV) in narrow cuts oriented NS ( $PA=2^\circ$ ) to better compare the shapes and distributions of X-ray and optical line emission. (*Bottom*) Corresponding cuts in the EW direction. The location of the cuts is indicated in Fig. 5. A  $15''$  wide cut was made in all cases. Each step in the EPIC-MOS data corresponds to  $\sim 5''$  and  $\sim 2.5''$  in the *Chandra* data. All data are normalized to the peak at  $0''$ , so that shapes are directly comparable. Regions A and B in Fig. 5 are identified in the top panels while the bottom ones are centered on A. The negative values in the  $H\alpha$  data are due to subtraction of the NGC 7318a/b nuclei. The higher resolution in the *Chandra* data is apparent and distinguishes the different features better, even at the degraded resolution used for this plot. The XMM-Newton data provide an important confirmation of the extent of the emission.

surface, but the density would suddenly change. Since these discontinuities are generally unstable, their presence might be understood if there is a magnetic field present that could suppress Kelvin-Helmholtz type instabilities generated by tangential flows. The detection of a radio continuum emission coincident with the shock front is evidence for the presence of a magnetic field (Williams et al. 2002; Xu et al. 2003). The  $H\alpha$  boundary at the same position and with a similar drop would need to be explained in the same context.

A close connection could also exist between the X-ray and dust distributions. Xu et al. (2003) have emphasized the role of dust in the cooling process behind the shock front resulting

from the collision between the intruder galaxy and SQ IGM. They argue that it could dominate the radiative cooling process. Residual  $60\ \mu\text{m}$  and  $100\ \mu\text{m}$  emission detected with ISO (i.e., not attributed to NGC 7319 and the foreground NGC 7320) shows an elongated feature coincident with the ridge observed in  $H\alpha$ , radio continuum, and X-ray (see Fig. 3 in Xu et al.). Xu et al. (2003) interpret this as evidence for shock-related Far InfraRed emission. They derive a sputtering timescale for the dust of a few times  $10^6$  yr, which is comparable to the timescale for gas cooling due to collision with dust grains. In their model, the expected luminosity for the dust is also comparable to the observed FIR luminosity attributed to the

shock region. Since the parameters assumed in Xu et al., based on our Chandra observation, are basically confirmed by the present XMM-Newton data, we do not recalculate these estimates. However, to properly interpret the exact role of the dust emission in the cooling process, and discard other plausible interpretations (e.g. evaluate the possible contribution from the unshocked arm of the new intruder along the same line of sight), a detailed comparison between the dust distribution and the X-ray emission in this region is required, together with a detailed treatment of the shock physics through, e.g., numerical simulations. The complexity of the multiphase medium that XMM-Newton data have shown will also have to be taken into account in any detailed modeling.

The spectral properties of the shock region are not well defined but, under the assumption of low metal abundance, imply a multi-temperature plasma. This is most likely the observational signature of non-equilibrium effects. Due to the differences in *atomic cross-sections* for ionization and recombination of different ions and ionization stages of the same ion, their coexistence in a plasma can mimic the signature of a multi-temperature structure. The assumption of equilibrium conditions, which is implicit in current plasma models, applies when the ionization and recombination time scales of the plasma are short compared to the dynamical and cooling time scales. This is not the case for recently shocked gas. Conversely, if the plasma is expanding rapidly due to its overpressure with respect to the ambient medium, recombination is expected to be delayed (Breitschwerdt & Schmutzler 1994, 1999). Unfortunately, lack of detailed knowledge of the gas dynamics and thermal history in SQ, coupled with the limitations of the data, prevents us from applying a proper modeling to account for non-equilibrium conditions.

Moreover, we cannot discard additional effects due to an inhomogeneous matter distribution and/or geometrical effects. The middle condensation (A) with smallest  $N_{\text{H}}$  could represent the leading edge of the approaching shock, already past the SQ debris field that is visible through  $\text{H}\alpha$ + $[\text{N II}]$  emission. The other two regions B and C might lag behind and still be embedded in molecular gas responsible for additional absorption. The neutral hydrogen detected in these regions is not enough to explain the inferred absorbing column densities. In fact no HI is detected in the region covered by our ellipse (Williams et al. 2002), although HI features are found at the N and S end with velocities consistent with those in the shock. We have interpreted the HI clouds and NS shock feature as evidence for a preexisting tidal feature possibly produced in earlier tidal activity (Sulentic et al. 2001; Trinchieri et al. 2003). The center of this feature is now shocked as a result of the recent collision with the new intruder. Evidence for a significant amount of debris, traced by the  $\text{H}\alpha$  emission, implies the presence of associated material, which could explain the higher absorption in X-rays.

As already discussed in the context of *Chandra* results (Trinchieri et al. 2003), the temperatures associated with pre- and post-shock medium are a problem in our current understanding of shocks and of the physical conditions of SQ: a bow-shock cannot be avoided if the new intruder slams into the debris with supersonic velocity, but the measured

temperatures are lower than what is expected from the velocity of the intruder. If the gas ahead of the shock is fairly hot, the shock Mach number is low ( $M = 2-3$ ), resulting in a low compression factor and a moderate increase in the post-shock temperature (2–4 times). With the limitation of the current spectral analysis, we measure a pre-shock temperature of  $\sim 0.3-1$  keV in “HALO” and “TAIL” which would imply a post-shock temperature in the range 1–4 keV. In shock, we measure  $kT \sim 1$  keV, at the lower end of the expected range, although a hint of higher temperatures is seen in the middle blob (see Table 3). We could, of course, be observing the system some time after the collision, after significant cooling has already occurred; however, the “radiative” cooling times that we derive,  $10^8-10^9$  yr, are long compared to the estimated crossing time for NGC 7318b and would further imply that the galaxy is now at a distance of several kpc from the site of impact. As suggested in Trinchieri et al. (2003), if the shock is oblique, most of the gas passes through the wings of the bow-shock under some angle, and hence compression and heating are reduced. Alternatively, if the gas has been freshly shocked, with ionization lagging behind the entropy increase, the post-shock gas appears to be “under-ionized”; i.e., it has essentially the same spectral characteristics as the unshocked medium. In this non-equilibrium ionization scenario, compression could be high, but we could still derive “low temperatures”. In this case, we have to be in a situation where the shock is very recent, because as time goes by the system would gradually be getting back to equilibrium conditions. If cooling by dust is a contributing or even dominant process, then the timescale for the shock could be extremely short, down to a few  $\times 10^6$  yr (Xu et al. 2003). In this case, if the cooling and sputtering times are comparable, the process could be self-regulating and result in an almost iso-thermal shock, explaining the lack of a temperature increase in the region.

### 3.3. Separating shocked and diffuse X-ray components in SQ

The analogies that compact groups show to rich clusters (e.g. extreme densities with resultant strong galaxy harassment) have led to claims that compact groups also typically show diffuse X-ray haloes. If primordial or at least virialized, they offer an important chance to map the gravitational potential of the aggregate. Several examples of X-ray clouds are found in compact groups. Hickson 62 represents probably the most unambiguous example of such a component, but lower luminosity and less massive examples have been found in other compact groups mostly with low spiral fraction (Mulchaey et al. 2003; Osmond & Ponman 2004). In the case of SQ, our inferences about any long-lived diffuse component have been clouded by the strong and complex emission from the large scale shock. Low resolution ROSAT-PSPC and ASCA observations were interpreted as emission dominated by a diffuse component (Sulentic et al. 1995; Awaki et al. 1997). Subsequent ROSAT-HRI and *Chandra* observations (Pietsch et al. 1997; Sulentic et al. 2001; Trinchieri et al. 2003) showed that most of the diffuse photons originated from the extended

shock, leaving little flux that could be ascribed to diffuse emission. XMM-Newton observations reported here provide the strongest evidence for diffuse emission in SQ, because the observed extent of the X-ray emission exceeds any reasonable estimate for the extent of shock related activity.

Spectral data for the extended emission also require a multi-component plasma model in analogy with the shock region. In fact there seems to be a continuity in the spectral properties out to the TAIL region. The surrounding region is apparently inhomogeneous like the shock front with a highly variable  $N_{\text{H}}$  column and an unrelaxed diffuse component mixed with emission related to the ongoing shock. The complex HI distribution in SQ may create or enhance the observed inhomogeneities. There are two X-ray components that we would like to separate: 1) shock related emission, very likely concentrated near the NS feature where, however, emission related to the shock proper, the new intruder disk, and a longer-lived diffuse component are probably mixed, and 2) the longer-lived diffuse component itself, of lower surface brightness and larger distribution. We will make use of the narrow band  $\text{H}\alpha + [\text{NII}]$  and broad  $R$  band images to respectively infer the extent of shock and diffuse emission components.

The 1D EW cuts shown in Fig. 9 indicate a significant extension towards the E in both line and X-ray emissions. The eastward extension is more significant in the new XMM-Newton data and can be traced up to  $60\text{--}70''$  ( $\sim 40$  kpc) east from the shock front and enveloping the Seyfert nucleus of NGC 7319. A similar diffuse extension up to  $\sim 50''$  is observed in line emission. Emission westward of the NS shock front is also visible in X-ray (mostly XMM-Newton) data, but at a lower intensity (see also Fig. 5 in Trinchieri et al. 2003).  $\text{H}\alpha + [\text{NII}]$  cannot be reliably mapped here because of problems associated with subtraction of the continuum emission near the centers of NGC 7318ab. The simplest interpretation sees the eastern emission extension as related to the new intruder disk. It may be the signature of a shocked eastern half of the disk, which is reasonable because almost no signature of neutral or warm gas is found eastward of the shock front indicating that the disk has already passed the front. On the contrary, two HI and numerous HII regions with new intruder velocities are observed west of the shock front. This east-west difference suggests that either the western side of the new intruder disk encountered much less SQ gas in its path or that it has not yet passed through SQ. The former appears likely, because the HI and HII associated with the western side indicate that the disk is disrupted. The high line of sight velocity of the intruder makes this disruption difficult to explain with a response time of  $t < 10^8$  years. It is difficult to infer a total luminosity for the shock related component. The bulk of the shocked emission is inferred to follow the contours superimposed on Fig. 8-right, where diffuse (assumed to be forbidden [NII]) line emission is found. It is the most reasonable approach we can take, given the complexity of the source, and it is reasonable to say that it is on the order of  $\sim 10^{41}$  erg  $\text{s}^{-1}$ , which would be high for a normal spiral unless enhanced by a collision.

Low level emission west of the shock front, as well as extended emission towards the SE (TAIL) and SW (towards

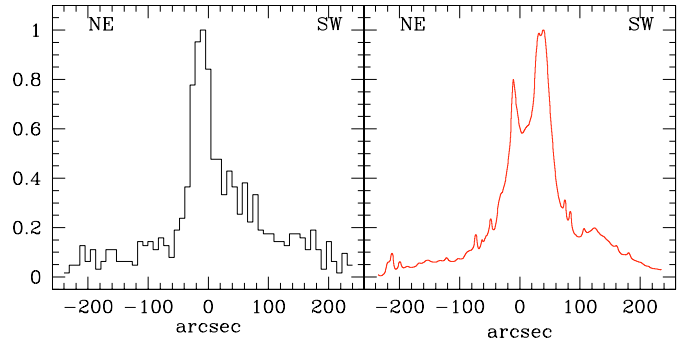


**Fig. 10.** Cut along the outer regions of the X-ray (*left*) and red continuum (*right*) emission (see Fig. 5), again normalized to their respective peaks. Each step in the EPIC-MOS data corresponds to  $\sim 7''$ . In both figures emission sloping to the SW is visible.

NGC 7317), are the strongest evidence for large scale diffuse X-ray emission in SQ (see Fig. 1 and Fig. 3). The irregular shape of this component suggests that it is far from dynamically relaxed. An optical or an X-ray diffuse halo will grow by sequential stripping in a compact group like SQ. Earlier analysis of optical data (Moles et al. 1998) showed a halo luminosity  $L \sim L^*$  and suggested a smoother distribution of diffuse light towards the west and a very complex distribution towards the east. The latter was interpreted as evidence for the most recent halo building event connected to the last passages of NGC 7320c and stripping of NGC 7319. The halo building component involves the optical tidal tails and associated debris between NGC 7319 and NGC 7320c. Star formation condensations have also been found in this debris many tens of kpc from group members/intruders (Sulentic et al. 2001; Mendes et al. 2005). Recent ultra-deep CCD imagery (Gutiérrez et al. 2002) considerably expands the size of the detected optical halo reinforcing the earlier conclusion that it represents an even more significant luminosity, and hence baryonic mass, component than previously estimated.

The 2D extent of the diffuse emission in both X-ray and optical light can be inferred from Fig. 1 and the comparison shown in Fig. 4 (X-ray contours on red image, left, and optical contours on X-ray color image, right). There is again a striking correspondence between diffuse emissions from hot gas and the stellar envelope in the southern half. Incidentally, this makes a strong case for the dynamical involvement of NGC 7317 in SQ (see Moles et al. 1998). An extension towards NNE is also seen in both X-ray and optical light (however, beware of the prominent Seyfert nucleus in the X-ray image). This extended emission cannot reasonably be ascribed to the ongoing shock and was apparently produced in earlier collisions within SQ that are hard to reconstruct now. The lobe-like structures are possible signatures of particular stripping episodes that have not had time to relax. The latest stripping episode involving debris towards the old intruder is even less relaxed and therefore more directly traceable to the last one or two intrusions of NGC 7320c. SQ is apparently an example of extensive diffuse light in a dynamically active compact group.

Figure 10 shows a further comparison between X-ray and red continuum emission intended to show the extent of diffuse emission towards the SW and NE directions. The 1D track is also shown in Fig 5, which is centered roughly SE of feature C. Unlike Fig. 9, the shapes of the two distributions are not similar. The “two-horned” profile in red continuum light is due to NGC 7318, while the peak in the X-ray plot is due to feature C and the bridge that connects it to the NS shock front. However diffuse emission can be traced in both plots out to at least to 200'' (70 kpc) SW and  $\sim 100''$  to the NE. This again indicates that the extended optical halo shows a correspondence with the extended X-ray halo. It is difficult to say more about the multiphase IGM of SQ especially in the absence of 3D data. An estimate for the X-ray luminosity of the (non-shock) diffuse emission yields  $L_x \sim 5 \times 10^{41} \text{ erg s}^{-1}$  (0.5–2 keV) comparable to the shocked component but of much lower surface brightness. It is also comparable to luminosities of the hot gaseous component in other low velocity dispersion groups discussed by Helsdon et al. (2005). SQ is a very low velocity dispersion group if the new intruder is not included in the estimate.

#### 4. Conclusions

*Chandra* and XMM-Newton have provided complimentary insights for the complex X-ray emission from Stephan’s Quintet. The strongest point source involves the Seyfert nucleus of NGC 7319 although all members have now been detected, except for the two intruders NGC 7320c and NGC 7318b. The most unusual aspect of the X-ray emission from SQ involves its extended emission. All of the galaxies in SQ have been stripped by a continuing sequence of intrusions by neighboring and possible member galaxies. The most recently stripped spiral galaxies involve NGC 7319 and NGC 7320c. Apparently enough gas was channeled into the nucleus of the former to stimulate an AGN, while the latter is undetected at all but optical wavelengths. The stripping events have given rise to a complex multiphase medium that has now been detected in radio continuum, radio lines (HI+CO), optical line ( $H\alpha$ +[N II]), and X-ray. Much/most of the radio continuum, optical line and X-ray emission are connected to a large scale shock generated by the most recent collision involving the ISM of NGC 7318b and the preexisting IGM debris field from previous stripping events. We infer an extent for the shock-dominated emission in excess of  $D \sim 50 \text{ kpc}$ . The stronger emission involves a narrow NS shock front that may reflect the existence of an extended debris field connecting two HI clouds in the new intruder path. The more extended shock-related emission is interpreted as the shocked new intruder disk. The 2D correspondence between the X-ray and optical line emission suggests a common origin for these two gas phases.

We now detect a much more extended ( $D \sim 130\text{--}150 \text{ kpc}$ ) diffuse component that cannot be ascribed to the shock. This is presumably related to the diffuse components found in other groups and clusters. Diffuse light from a halo of stripped stars maps this X-ray structure. The complex lobe-like structure of this halo presumably reflects a group far from a state of dynamical relaxation.

It is difficult to find an analogy to SQ in the current X-ray literature. The closest might be the Antennae (Fabbiano et al. 2003; Metz et al. 2004), where strong interactions have obviously taken place. However the analogy quickly breaks down, because the Antennae are dominated by star formation regions, and most of the diffuse X-ray emission is associated with these regions. In addition, while strongly distorted, most of the gas still resides in the galaxies. We do not see evidence for widespread star formation activity in SQ galaxies, although we see small star-forming condensations developing in the stripped debris (Xu et al. 1999; Sulentic et al. 2001; Mendes et al. 2005). Shocked emission in SQ does not follow these few features: it is concentrated in a more localized region presumably at the sight of current impact and appears to be more extended than traced by the  $H\alpha$  emission (although mixing with the pre-existing diffuse emission might play a role). The spectra of the diffuse components in SQ and the Antennae both require multi-temperature fits; however, it is very likely that this is just the observational signature of very complex temperature distributions and/or non-equilibrium effects. In the Antennae, a detailed analysis has shown the presence of regions at different temperatures and absorption depths (Fabbiano et al. 2003). In SQ we both have evidence of condensations at different temperatures and expect non-equilibrium conditions. Unfortunately, current observations do not allow us to calculate the dynamics and the thermal history of the plasma self-consistently, so as to properly model its physical conditions.

*Acknowledgements.* We thank the referee, Dr. C. Xu, for pointing out to us the relevance of dust cooling in the shock region and for several useful comments that helped improve the paper. This research made use of SAOImage DS9, developed by the Smithsonian Astrophysical Observatory. GT acknowledges partial financial support by the Italian Space Agency ASI. JS acknowledge NASA support under contract NAG5-11204. We thank Carlo Gutierrez for making his optical *R*-band data available.

#### References

- Awaki, H., Koyama, K., Matsumoto, H., et al. 1997, PASJ, 49, 445
- Bekki, K., & Couch, W. J. 2003, ApJ, 596, L13
- Breitschwerdt, D., & Schmutzler, T. 1994, Nature, 371, 774
- Breitschwerdt, D., & Schmutzler, T. 1999, A&A, 347, 650
- della Ceca, R., Castelli, G., Braito, V., Cagnoni, I., & Maccacaro, T. 1999, ApJ, 524, 674
- Fabbiano, G., Zezas, A., & Murray, S. S. 2001, ApJ, 554, 1035
- Fabbiano, G., Krauss, M., Zezas, A., Rots, A., & Neff, S. 2003, ApJ, 598, 272
- Fujita, Y., & Nagashima, M. 1999, ApJ, 516, 619
- Galianni, P., Burbidge, E., Arp, H., et al. 2004 [arXiv:astro-ph/0409215]
- Gallagher, S. C., Charlton, J. C., Hunsberger, S. D., Zaritsky, D., & Whitmore, B. C. 2001, AJ, 122, 163
- Gutiérrez, C. M., López-Corredoira, M., Prada, F., & Eliche, M. C. 2002, ApJ, 579, 592
- Helsdon, S. F., Ponman, T. J., & Mulchaey, J. S. 2005, ApJ, 618, 679
- Hickson, P. 1982, ApJ, 255, 382

- Jog, C. J., & Solomon, P. M. 1992, *ApJ*, 387, 152
- Mazzotta, P., Fusco-Femiano, R., & Vikhlinin, A. 2002, *ApJ*, 569, L31
- Mendes, C., Coelho, P., González, J., & Barbuy, B. 2005, *AJ*, 130, 55
- Metz, J. M., Cooper, R. L., Guerrero, M. A., et al. 2004, *ApJ*, 605, 725
- Moles, M., Marquez, I., & Sulentic, J. W. 1998, *A&A*, 334, 473
- Moran, E. C., Kay, L. E., Davis, M., Filippenko, A. V., & Barth, A. J. 2001, *ApJ*, 556, L75
- Mulchaey, J. S., Davis, D. S., Mushotzky, R. F., & Burstein, D. 2003, *ApJS*, 145, 39
- Osmond, J. P. F., & Ponman, T. J. 2004, *MNRAS*, 350, 1511
- Pietsch, W., Trinchieri, G., Arp, H., & Sulentic, J. W. 1997, *A&A*, 322, 89
- Roberts, T. P., & Warwick, R. S. 2000, *MNRAS*, 315, 98
- Sulentic, J. W., Pietsch, W., & Arp, H. 1995, *A&A*, 298, 420
- Sulentic, J. W., Rosado, M., Dultzin-Hacyan, D., et al. 2001, *AJ*, 122, 2993
- Trinchieri, G., Sulentic, J., Breitschwerdt, D., & Pietsch, W. 2003, *A&A*, 401, 173
- van der Hulst, J. M., & Rots, A. H. 1981, *AJ*, 86, 1775
- Vikhlinin, A., Markevitch, M., & Murray, S. S. 2001, *ApJ*, 551, 160
- Williams, B. A., Yun, M. S., & Verdes-Montenegro, L. 2002, *AJ*, 123, 2417
- Wolter, A., & Trinchieri, G. 2004, *A&A*, 426, 787
- Xanthopoulos, E., Muxlow, T. W. B., Thomasson, P., & Garrington, S. T. 2004, *MNRAS*, 353, 1117
- Xu, C., Sulentic, J. W., & Tuffs, R. 1999, *ApJ*, 512, 178
- Xu, C. K., Iglesias-Páramo, J., Burgarella, D., et al. 2005, *ApJ*, 619, L95
- Xu, C. K., Lu, N., Condon, J. J., Dopita, M., & Tuffs, R. J. 2003, *ApJ*, 595, 665
- Zezas, A., & Fabbiano, G. 2002, *ApJ*, 577, 726
- Zezas, A. L., Georgantopoulos, I., & Ward, M. J. 1999, *MNRAS*, 308, 302